Applied Surface Science 464 (2019) 61–67

Contents lists available at ScienceDirect

Applied Surface Science

journal homepage: www.elsevier.com/locate/apsusc

Full Length Article

Large and constant absorption coefficient in $Nb_xTi_{1-x}O_2$ thin films throughout the visible range

Adam E. Shimabukuro[b], Akihiro Ishii[a], Itaru Oikawa[a], Yusuke Yamazaki[c], Masaaki Imura[c], Toshimasa Kanai[c], Fumio S. Ohuchi[b], Hitoshi Takamura[a,*]

[a] Department of Materials Science, Graduate School of Engineering, Tohoku University, Sendai 980-8579, Japan
[b] Department of Materials Science and Engineering, College of Engineering, University of Washington, Seattle 98195, USA
[c] Thin Films Division, Nippon Electric Glass Co., Ltd., Nagahama 529-0292, Japan

ARTICLE INFO

Keywords:
Pulsed laser deposition
Non-dispersive media
NbO_2
Ti_4O_7
Absorption coefficient

ABSTRACT

We investigated the optical absorption properties of $Nb_xTi_{1-x}O_2$ thin films, a solid solution combining the reduced titanium and niobium oxide phases TiO_2 and NbO_2. The optical absorption properties of $Nb_xTi_{1-x}O_2$ thin films prepared by pulsed laser deposition at 600 °C were shown to be large in magnitude at an almost constant value of $\approx 17\ \mu m^{-1}$. Because this large absorption coefficient is nearly independent of incident photon energy in the visible range (400–700 nm), the $Nb_xTi_{1-x}O_2$ thin films appear optically black. Flat and homogenous, optically black coatings like these are desirable for color isolation in flat panel displays. The origin of flat wavelength dispersion in $Nb_xTi_{1-x}O_2$ is the coexistence of semiconducting absorption and metallic light absorption mechanisms. Localized Nb-Nb dimers in the metallic $Nb_xTi_{1-x}O_2$ phase open an optical band gap which gives rise to semiconducting behavior. We show here that reduction results in strong visible light sensitization in normally transparent Nb-Ti oxides.

1. Introduction

Optically absorbing coatings are important for applications both future and present in the electronics display industry. Organic light-emitting displays (OLED) and liquid crystal displays (LCD), for example, require a black matrix coating to optically isolate the colors of individual pixels. Displays with good isolation have superior contrast and can display dark colors. The black matrix also dictates the powered-off appearance of these displays. Ideal coatings for this application must meet two important criterion:

(1) They must be homogeneous and flat to avoid light scattering and for compatibility with layered structures.
(2) They must have a large, consistent absorption coefficient, α(E) to ensure wavelengths in the visible light region are absorbed with constant intensity.

Materials with such dispersion behavior appear exceptionally black. Organic molecules with a variety of bond lengths and vibrational modes are known to absorb many wavelengths of light in the visible spectrum [1,2]. Therefore, visible light absorbing coatings are typically made from organic resins and pigments. However, organic compounds have poorer thermal stability and resistance to ultraviolet radiation than inorganic metal oxides. Additionally, metal oxide coatings are compatible with many existing mass production facilities. A novel visible-light-absorbing oxide film with flat wavelength dispersion should be the key to improving the picture quality of LCD and OLED displays. It may be possible to achieve such flat wavelength dispersion in metal oxides by combining an oxide with strong short wavelength absorption with another oxide which has strong long wavelength absorption. Short wavelenth absorption known as Tauc absorption [3–5] is typically applied to semiconductors while long wavelength absorption is known as Drude absorption [3,6,7] is typical of metals.

It is known that oxygen vacancies increase optical absorption in metal oxides by introducing free carriers and mid-gap defect levels [8–10]. A large amount of reduction has been show to lead to the periodic ordering of oxygen vacancies in the form of crystallographic shear planes [11]. For example, the Magnéli Ti_nO_{2n-1} series crystallizes into distorted rutile structures with shear planes along a pseudo-rutile *c* axis where edge-sharing octahedra become face-sharing in order to accommodate reduced Ti^{3+} cations [12,13]. These phases are considered metallic as their Fermi energies lie just below their conduction bands [14]. Accordingly, Magnéli titanium oxides exhibit free carrier conductivity and optical absorption. This optical absorption is strongest

* Corresponding author.
E-mail address: takamura@material.tohoku.ac.jp (H. Takamura).

https://doi.org/10.1016/j.apsusc.2018.09.036
Received 24 May 2018; Received in revised form 23 August 2018; Accepted 5 September 2018
Available online 06 September 2018
0169-4332/ © 2018 Elsevier B.V. All rights reserved.

in the long wavelength near infrared region.

Another oxide with metallic behavior is NbO_2. NbO_2 is particularly interesting because it undergoes a transition from an insulating phase to a metallic phase at around 800 °C [15–17]. This transition is accompanied by a transformation from distorted rutile type to regular rutile type. In the insulating phase, alternating short (2.7 Å) and long (3.3 Å) Nb-Nb dimers exist along the *c* axis [17]. The alternating bond length of these dimers gives rise to a Peierls type instability along the *c*-axis by changing domians of periodic potential in the lattice, causing an insulator to metallic transition [15,17,18]. The instability opens an appreciable band gap of indirect nature by splitting the Nb-4d bands [17,18]. While the exact value of this gap is unclear, calculations have evaluated it as low as 0.1 eV and spectroscopy measurements as high as 1.3 eV have been reported [15,16,18,19]. The transformation from insulator to metal is based on the thermal dissolution of long Nb-Nb dimers [20]. Sakata found that over a large composition range, Nb and Ti form a solid solution of $Nb_xTi_{1-x}O_2$. From $0 < x < 0.85$, the solid solution is metallic rutile type at temperatures as low as 500 °C [20,21]. Because the closed shell Ti structure is less likely to dimerize than open shell Nb^{4+}, the introduction of Ti lowers the transformation temperature from insulating to metallic. Sakata also reported a nonlinear increase in the *c* axis, with $0 < x < 0.85$ indicating the persistence of some short Nb-Nb dimers. The existence gap forming short Nb-Nb dimers in a metallic phase makes the $Nb_xTi_{1-x}O_2$ system an excellent candidate for a film that displays both long and short (Drude and Tauc) wavelength absorption. However, the optical properties of this solid solution have not been reported. Here we show that the optical absorption of $Nb_xTi_{1-x}O_2$ is characteristic of both short wavelength indirect gap absorption and long wavelength free carrier absorption. It is also shown that redox interactions between Nb and Ti occur in the solid solution.

2. Experimental

Films were synthesized by pulsed laser deposition (PLD). PLD targets were prepared using Nb(V) oxide powder (Kanto Chemical Ltd.: purity 99.95%) and rutile Ti(IV) oxide powder (High Purity Chemical Ltd.: purity 99.9%). Four targets, TiO_2, Nb_2O_5, and $TiNb_2O_7$ and TiO_2-$TiNb_2O_7$ composite (25 cationic mol% Nb), were prepared by solid state reaction at 1250 °C. All films were deposited on amorphous alkali-free glass (OA-10G, Nippon Electric Glass Co., Ltd.: 15 mm × 15 mm × 0.5 mm) using a KrF excimer laser (COMPex-Pro205, COHERENT, Inc,: λ = 248 nm) repeated at 5 Hz for 30 min with a laser fluence of 5.8 Jcm^{-2}. The deposition chamber (PLAD-242, AOV Co., Ltd.) was evacuated to an atmosphere of $< 10^{-4}$ Pa. This vacuum condition was required in order to obtain NbO_2 rather than Nb_2O_5 and substoichiometric TiO_{2-x} rather than TiO_2. The glass substrates were heated to 600 °C by means of an infrared heating lamp. This temperature was chosen because the phase study reported by Sakata indicates both insulating NbO_2 and metallic $Nb_xTi_{1-x}O_2$ are stable at this temperature [20,21]. Films deposited at 600 °C under a high vacuum were between 35 and 50 nm in thickness.

The structure of the as deposited films were characterized with grazing incidence X-ray diffraction (D8 Advance, Bruker AXS) with a grazing angle of 2° with a Cu-Kα radiation source (λ = 1.5418 Å) and Raman spectroscopy (HR-800, Horiba Jobin Yvon S.A.S.) using a He-Ne laser (λ = 632.8 nm). Surface morphology and average roughness were measured by atomic force microscopy (AFM) (AFM, JSPM-5200. JEOL Ltd.). The chemical states were measured using an XPS (Theta Probe, Thermo Electron Corporation) with an Al-Kα source (λ = 1486.6 eV) from a flood type electron gun and spectroscopic ellipsometry (M-2000, J.A. Woollam Co., Ltd.). Due to the insulating nature of the sample surfaces, XPS peak positions were corrected using a carbon 1 s reference set at 285.00 eV. Gauss-Lorentz deconvolution was used for Nb-3d peaks. This fitting employed several fixed parameters; between the 5/2 and 3/2 peaks the area ratio and energy separation were fixed. Ti-2p peaks were deconvoluted using a rutile powder reference sample. An Nb-3 s peak near 470 eV was included in the Ti-2p peak deconvolution in order to obtain an accurate fit for samples containing both Nb and Ti.

Table 1
Naming conventions for thin films and the compositions of their PLD targets.

Sample	Cationic mol% Ti in targets	Cationic mol% Nb in targets	Deposition Temperature [°C]
T100	100	0	600
TN25	75	25	600
TN67	33	67	600
N100	0	100	600

Spectroscopic ellipsometry was used to obtain the optical properties of the film. Measurements of the phase and amplitude changes, Δ and ψ were obtained at 50° and 70° from normal at a spectral range of 250–1000 nm. Our model included a 0.5 mm Cauchy film as the substrate, the deposited film and an air layer. The complex pseudo-dielectric function was modelled from this data and the refractive index (n) and extinction coefficient (k) were derived from this function. The absorption coefficient is defined by $\alpha = 2\pi k/\lambda$. A multi oscillator scheme was used to model the dielectric functions of the films. Tauc-Lorentz oscillators were used throughout except for the near infrared region of the T100. A metallic type Drude oscillator was used for this region because of its good fit to the data. In every case, the model obtained a mean squared error below 10. The compositions of the deposited films and the naming conventions are summarized in Table 1. The films are referred to by these names hereafter.

3. Results and discussion

The films were deposited under a high vacuum in order to introduce oxygen vacancies and reduce the oxide cations for visible light sensitization. While stoichiometric TiO_2, Nb_2O_5 and Nb^{5+} doped TiO_2 are typically transparent the results of this study show that reduction is highly effective to sensitize these oxides to visible light [16,22–25]. Since the films deposited at lower than 600 °C were largely amorphous, only polycrystalline films deposited at 600 °C were used in this study. Grazing incidence XRD and Raman spectroscopy were used for structural characterization and phase identification; these spectra are shown in Fig. 1.

The XRD spectrum of the N100 film deposited under high vacuum at 600 °C was indexed to distorted rutile type ($I4_1/a$) NbO_2. This is the insulating phase of this film, its XRD spectrum is shown in Fig. 1a. T100 was largely amorphous due to deposition on the amorphous glass substrate, thus oxygen deficiency related stacking faults are randomly distributed throughout the film. However, the Raman spectrum of T100 shown in Fig. 1b, is consistent with the previously reported Raman spectra of Magnéli type Ti_4O_7 [13] indicating localized Ti_4O_7 coordination. While N100 was the low temperature insulating phase of NbO_2, the TN25 and TN67 films were indexed to the metallic regular rutile phase of $Nb_xTi_{1-x}O_2$ showin in Fig. 1a. The absence of the XRD peaks attributed to (1 0 1) and (2 1 1) planes might indicate a preferred orientation near the surface where grazing incidence XRD analyzes. This is likely because the planes perpendicular to the *c*-axis have lower surface energy than the other planes in the rutile type crystal structure [26]. The peaks of the Raman spectra of TN25 and TN67 films were identical at 304 and 722 cm^{-1}, as shown in Fig. 1b, and agree reasonably well with the Raman data reported for metallic rutile type NbO_2 [27]. Broadening of these Raman peaks can be attributed to the atomic displacement of Nb due to local dimerization. The Raman spectrum of our NbO_2 film matches previously reported data well [28]. The positions of the XRD peaks shown in Fig. 1a were used to calculate the *a* axis lengths of TN67 and TN25, at 4.783 Å and 4.728 Å, respectively. These values are consistent with the measurements of the *a* axis versus composition in $Nb_xTi_{1-x}O_2$ reported by Sakata [20]. Expansion

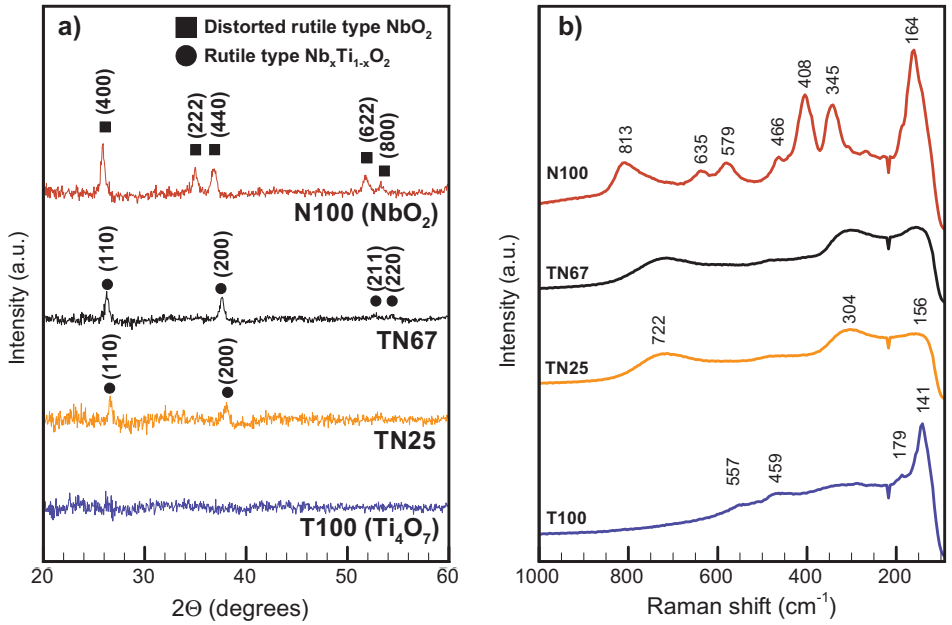

Fig. 1. Structural identification data. (a) Thin film XRD diffraction data with amorphous substrate background data subtracted, (b) Raman spectra of thin films. The diffuse peaks of TN67 and TN25 are caused by localized Nb-Nb dimers which inhibit long range order.

of the *a* axis with increasing Nb content is related to the incorporation of Nb in the lattice.

Since optical absorption is also dependent on surface roughness, we analyzed surface morphology with AFM. The air-oxide interface of very rough surfaces causes non specular absorption and reflection which does not represent the optical response of a film's bulk [29]. Atomic force microscopy analysis on our films yielded acceptable surface roughness values below 1 nm. TN25 had an average surface roughness of 0.51 nm while TN67 had an average surface roughness of 0.68 nm. Micrographs of the film surfaces are shown in Fig. 2. Such small surface deviations are not significant sources of error for our absorption measurements, and suggest these thin films are compatible with the layered structures.

Film absorption spectra obtained from spectroscopic ellipsometry and actual film appearances are shown in Fig. 3. N100 appears slightly red because of its strong absorption in the blue region but weak absorption in the red region. T100 appears slightly blue due to its strong red region absorption but weak blue region absorption. TN25 and TN67 have strong absorption in both blue and red regions and accordingly, the films appear black with no coloration. For these $Nb_xTi_{1-x}O_2$ thin films, no light scattering is visible and no surface roughness layers are required for the analysis with spectroscopic ellipsometry as indicated by the AFM images (Fig. 2). The variance in TN25 and TN67 absorption coefficient throughout the visible spectrum is in the range of 3 μm^{-1}.

The absorption spectra of our thin films was compared to Si, titanium nitride and Fe_3O_4 dispersion data from the literature [30–32]. Our experimental absorption spectra along with literature absorption spectra are plotted in the visible region in Fig. 4. From this image, it is clear that the absorption coefficients of both TN25 and TN67 are very large and almost constant. While the wavelength disperson of Fe_3O_4, which is used commercially as a black pigment, is also very flat, the magnitude of its absorption is very small [33].

Since absorption coefficient uniformity and magnitude are important characteristics of absorbing films, a numerical assessment of these quantities is required. We describe the magnitude of absorption spectra using the film absorption coefficient value at 550 nm, the wavelength at which the human retina is most sensitive [34]. The uniformity of a spectrum can be described quantitatively by the average deviation from the absorption coefficient at 550 nm. The average deviation is the absolute sum of deviations from the value at 550 nm normalized by the number of data points in the set. For this analysis, we used only data in the visible range (400–700 nm). These values are marked by colored squares in Fig. 4 and are tabulated numerically along with average deviations in Table 2. A material with 'blackness'

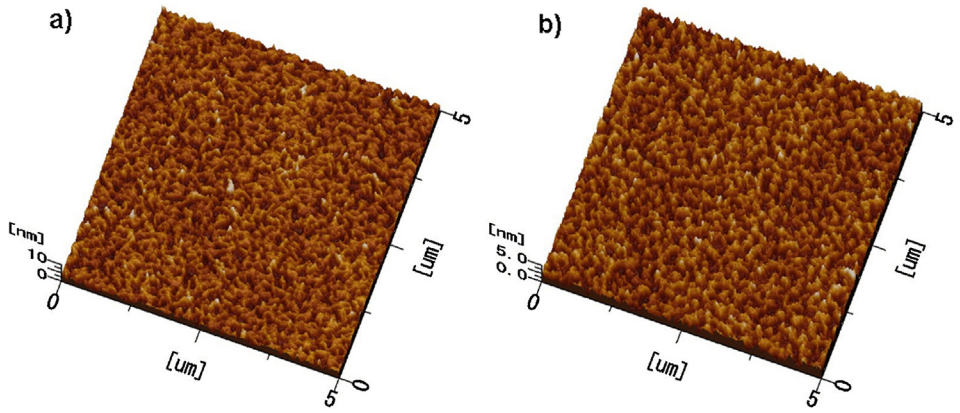

Fig. 2. AFM images of (a) TN67 and (b) TN25. In both cases, the average surface roughness in less than 1 nm.

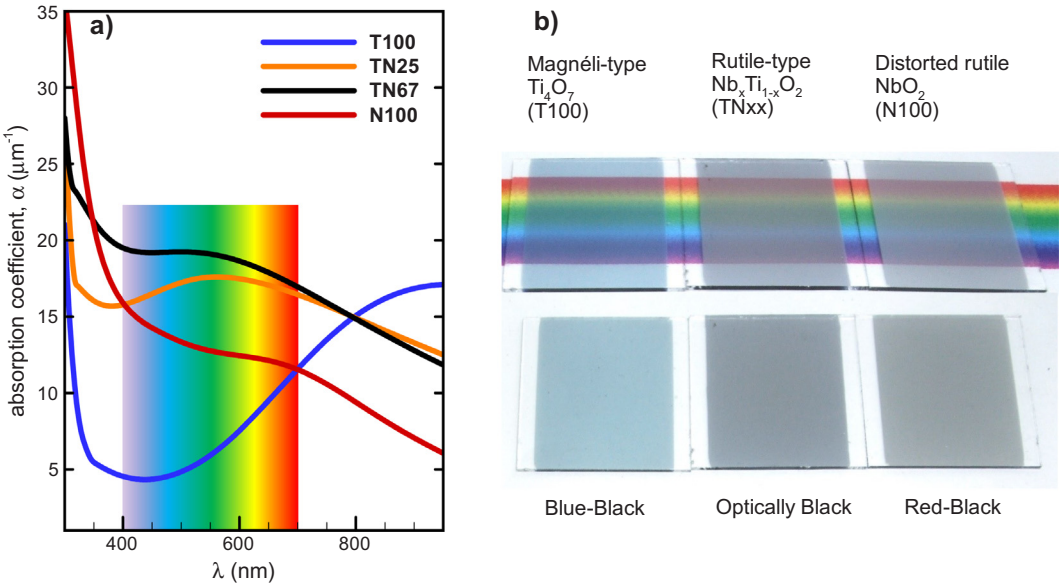

Fig. 3. (a) Absorption spectra derived from spectroscopic ellipsometry with the visible spectrum represented graphically. (b) Film appearance and color transmittance. TN67 and TN25 rutile type $Nb_xTi_{1-x}O_2$ films appear optically black because their absorption coefficients are almost constant in the visible spectrum.

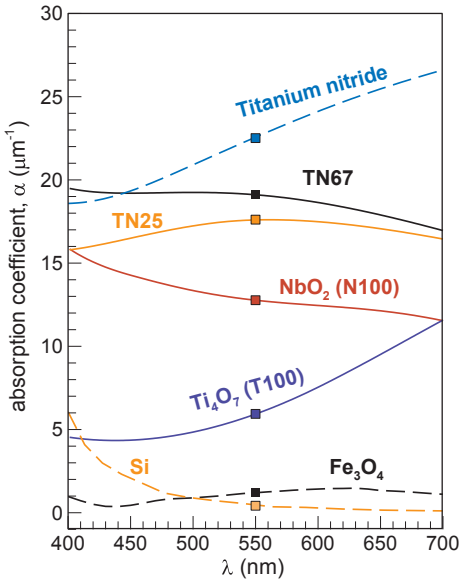

Fig. 4. Absorption spectra in the visible range from experimental (solid) and literature (dashed) data. Colored squares mark the absorption coefficient at 550 nm. (For interpretation of the references to colour in this figure legend, the reader is referred to the web version of this article.)

Table 2
Tabulated values for absorption coefficient at 550 nm and the average deviation within the visible range.

Material	Absorption coefficient at 550 nm, α(550 nm) [μm^{-1}]	Average deviation [μm^{-1}]
T100 (Ti_4O_7)	5.94	2.59
TN25	17.62	0.74
TN67	19.10	0.83
N100 (NbO_2)	12.77	0.96
Fe_3O_4 [24]	1.19	0.28
Titanium nitride [23]	22.51	4.64
Si [22]	0.42	1.21

suitable for the electronic display industry should have a large absorption coefficient at 550 nm with a small average deviation from that value. The large absorption coefficients, at 550 nm, of both TN25 and TN67 are comparable to that of metallic titanium nitride, and their small average deviations are comparable to Fe_3O_4. This analysis shows the rutile type $Nb_xTi_{1-x}O_2$ is an excellent candidate for optically black absorbing layers because of its large, almost constant absorption coefficient throughout the visible range.

The two primary mechanisms responsible for optical absorption near the band edge are the primary interband transition and transitions due to localized states. These localized transitions create Urbach tails and result in a smaller amorphous band gap than the crystalline band gap [35–38]. For the films deposited in this study, the absorption edge is outside the visible range, and the primary character we observe is the absorption tail. This is clear from the spectral shapes in Fig. 3a. The shapes of these tails is related to the electronic structure and the type of transition which results in the tails.

The metallic absorption tail can be clearly differentiated from the semiconducting tail. Tauc suggested the energy dependence of the absorption tail in amorphous semiconductors is $a(\omega)_{Tauc} \propto \omega^2$ [35]. Although it is only applicable to allowed type transitions in indirect gap semiconductors, this relationship has been used extensively to approximate the optical band gap with reasonable accuracy [3,39,40]. A similar relationship was later derived for indirect gap semiconductors with forbidden type transitions by Nakahara *et al.* where $a(\omega) \propto \omega^{\frac{1}{3}}$ near the absorption edge and $a(\omega) \propto \omega^{\frac{2}{3}}$ at lower energies [41]. It then follows that the absorption tail of indirect gap semiconductors increases with frequency, according to $a(\omega) \propto \omega^n$ where $n > 1$ or decreases with the wavelength, according to $a(\lambda) \propto \lambda^n$ where $n < 1$.

Because of their large free carrier concentration, the absorption tail energy dependence can also be derived for semiconductors which behave like metals [3]. Typically, the plasma frequency, ω_p, of metals is well into the ultraviolet region and reflectance is dominant in the visible range. However, for metal-like semiconductors, we can apply Drude conductivity, $\sigma_{Drude} = (ne^2\tau)/(m^*(1-i\omega\tau))$ to the complex dielectric function, $\varepsilon(\omega) = [\tilde{n}(\omega) + i\tilde{k}(\omega)]^2 = \varepsilon_c + 4\pi i\sigma/\omega$ where ω is incident angular frequency, τ is the scattering time, m^* is the effective mass, ε_c is the core polarizability, $\tilde{n}(\omega)$ and $\tilde{k}(\omega)$ are the complex refractive index and extinction coefficient, respectively. Given the relationship, $\alpha = (2\omega\tilde{k}(\omega))/c$ and assuming $\omega\tau$ is much larger than 1 in the visible range for a semiconductor with large free carrier

concentration, it can be concluded that very simplistic free carrier absorption in semiconductors is described qualitatively by $\alpha_{Drude}(\omega) \propto \omega^{-2}$ or $\alpha_{Drude}(\lambda) \propto \lambda^2$ [3].

From the spectra in Figs. 3a and 4, it is clear that Ti_4O_7 (T100) has a metal like absorption tail where α increases with wavelength. Similarly, metallic titanium nitride has an absorption tail which increases with wavelength. As expected, Si has a semiconducting band tail, and NbO_2 (N100), which is known to be an indirect gap semiconductor, also has a semiconducting band tail [15]. Since the Peierls gap in NbO_2 opens in the Nb-4d orbital, the transition should be forbidden [15,17,18]. Accordingly, the absorption tail of N100 appears to have two regimes of $a(\lambda) \propto \lambda^n$.

The absorption tails of the TN25, TN67 and Fe_3O_4 do not obey the aforementioned power laws. Optical absorption in magnetite Fe_3O_4 originates from distinct O-2p to Fe-4s and Fe-3d to Fe-4s transitions [42]. Furthermore, both Fe^{2+} and Fe^{3+} exist simultaneously [42]. The result is an absorption tail that is neither specifically semiconducting or metallic. We believe a similar duality is responsible for the optical absorption characteristics of rutile type $Nb_xTi_{1-x}O_2$ (TN25 and TN67). It is likely that a Peierls gap in the Nb-4d orbital in the metallic $Nb_xTi_{1-x}O_2$ phase gives the solid solution both semiconducting and metallic absorption. By tuning the Nb-Ti ratio and thus the amount of band opening Nb-Nb dimers, the uniformity of the visible range absorption spectra can be controlled.

Absorption in TN25 and TN67 films is more complicated than a simple mixture of N100 and T100. Using the measured absorption spectra of T100 and N100, the mole fraction was synthesized based on the addition absorption curves for TN25 and TN67. Curve synthesis for TN25 was carried out by scaling the absorption values of T100 by 75% and adding them to the values of N100 scaled to 25%. A similar procedure was used for TN67, using 33% and 67%, respectively. These synthesized curves are shown in Fig. 5. The deviation between measured absorption spectra and synthesized absorption spectra for TN25 and TN67 is likely due to slight oxygen non-stoichiometry and interactions between Nb and Ti cations.

XPS measurements gave insight into the chemical interactions taking place in the $Nb_xTi_{1-x}O_2$ solid solution. The integration of deconvolved metal peaks and O-1s peaks yielded average values for composition and cationic valencies. The calculated average chemical states of are as follows: T100 → $Ti^{3.35+}$, N100 → $Nb^{4.25+}$, TN67 → $Ti^{3.76+}$&$Nb^{4.33+}$. These values are in good agreement with the stoichiometry of the film phases: Ti_4O_7, NbO_2, $Nb_{.67}Ti_{.33}O_2$. Since the XPS measurent is a surface sensitive method, we expect the bulk to be more reduced than the measurements indicate. For example, the XPS spectrum of N100 shown in Fig. 6c exhibits a high concentration of Nb^{5+} which should not be present in NbO_2. This large concentration of Nb^{5+} must be due to film storage in open atmosphere.

XPS measurements were important to understand cationic interactions in $Nb_xTi_{1-x}O_2$. The Nb^{2+} state in TN67 not seen in N100 can be seen in Fig. 6. Additionally, more of the Ti cations were oxidized in TN67 than in T100. We see that Ti tends to reduce Nb in solution. This is likely attributed the formation of a fully coordinated Ti octahedron which is more energetically favorable than a fully coordinated Nb octahedron according to the reported free energy of formation values [43]. From the valency information alone, inferences can be made regarding the band structure of $Nb_xTi_{1-x}O_2$: namely, the conduction band consists of TiO_2-like Ti-3d orbitals, NbO_2-like Nb-4d orbitals and probably some hybridization of the two. Due to the contribution of Nb-Nb dimers, there is also a small gap in the conduction band. Combined, these conduction band features give rise to the non-typical absorption spectra of the TN25 and TN67 films. It is possible that other as-yet unknown chemical mechanisms are at play in the $Nb_xTi_{1-x}O_2$ solid solution. Some research has suggested Nb-Ti hybridization forms a non-bonding band near the valence band [44]. We can speculate that exotic orbital hybridizations or charge transfer complexes exist, but only in depth *ab initio* calculations can shed light on these processes.

4. Conclusion

We studied the optical absorption properties of the reduced titanium and niobium oxide phases Ti_4O_7 and NbO_2 as well as the solid solution of the two. The visible spectrum absorption coefficient power law, $\alpha(\lambda) \propto \lambda^n$ where $n = -2$ for semiconductors and $n = 2$ for metals applies reasonably well to insulating NbO_2 and metallic Ti_4O_7. The absorption spectra of solid solution $Nb_xTi_{1-x}O_2$ appears to be a combination of both types. Due to its large, nearly constant absorption coefficient throughout the visible range, this rutile type $Nb_xTi_{1-x}O_2$ is an excellent candidate for optically black absorbing layers. Localized Nb-Nb dimers in the metallic $Nb_xTi_{1-x}O_2$ phase open an optical band gap resulting in the coexistence of semiconducting and metallic absorption mechanisms in a single phase. The extent of this semiconducting and metallic character can be manipulated by controlling the Nb-Ti ratio. The Nb-Ti solid solution was found to be rather complex from an electronic perspective because of cationic reduction and

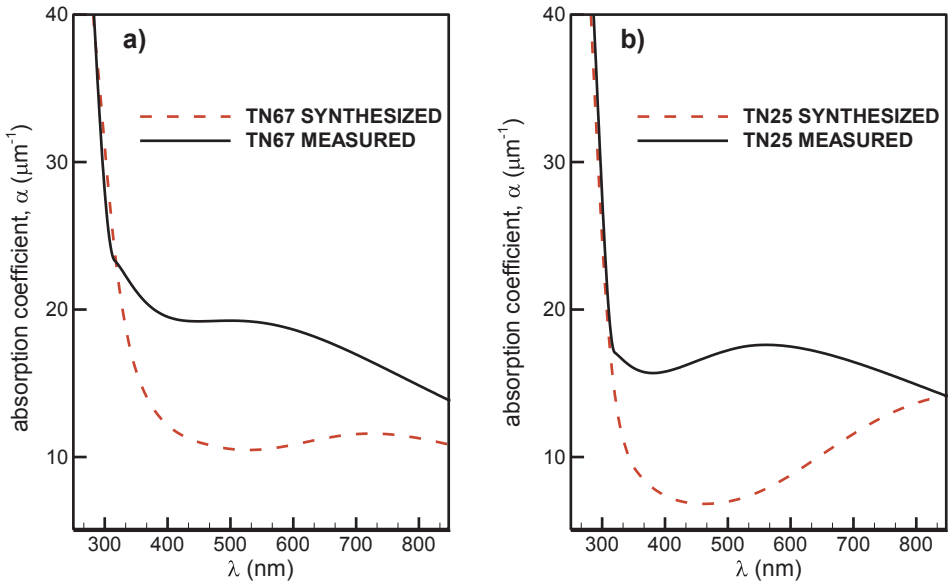

Fig. 5. Measured and synthesized absorption spectra for (a) TN67 and (b) TN25.

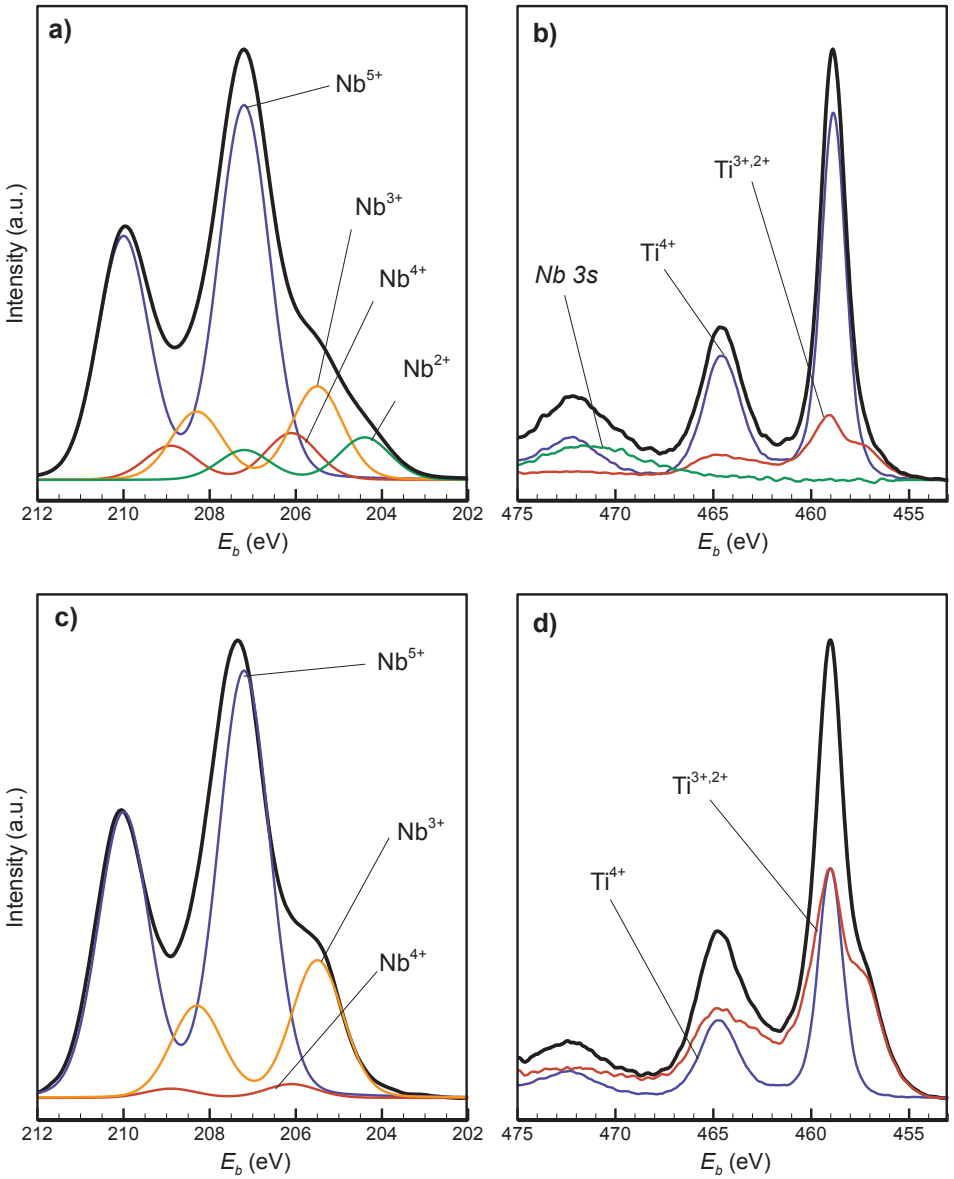

Fig. 6. XPS spectra of thin films (a) Nb-3d of TN67 (b) Ti-2p of TN67 (c) Nb-3d of N100 (d) Ti-2p of T100. In TN67, Nb is more reduced than in N100 and Ti is less reduced than in T100.

oxidation since Ti tends to reduce Nb. Due to this effect, the absorption spectra of the $Nb_xTi_{1-x}O_2$ is different from that of numerical combination of NbO_2 and Ti_4O_7. Further investigation is necessary to elucidate how this cation interaction impacts the band structure, and, in turn, the optical absorption properties of the solid solution.

Acknowledgments

This work has been financially supported in part by JSPS KAKENHI grant number 18H03832. AS would like to thank the research placement done by Junior Year Programs in English (JYPE) at Tohoku University. AI would like to express his appreciation for the financial from the Grant-in-Aid for JSPS Research Fellows and the Interdepartmental Doctoral Degree Program for Multi-dimensional Materials Science Leaders in Tohoku University. The authors would like to acknowledge the vitally important encouragement and support made through the University of Washington-Tohoku University: Academic Open Space (UW-TU:AOS). They also would like to thank Ms. Y. Ohira and Mr. N. Akao for technical support in taking XPS measurements.

References

[1] S. Bum Yuk, W. Lee, J. Woong Namgoong, J. Choi, J. Bok Chang, S. Hun Kim, J. Yun Kim, J. Pil Kim, Synthesis and characterization of bay-substituted perylene dyes for LCD black matrix of low dielectric constant, J. Incl. Phenom. Macrocycl. Chem. 82 (2015) 203–212.
[2] J. Choi, W. Lee, J.W. Namgoong, T.-M. Kim, J.P. Kim, Synthesis and characterization of novel triazatetrabenzcorrole dyes for LCD color filter and black matrix, Dye. Pigment. 99 (2013) 357–365.
[3] M. Dresselhaus, G. Dresselhaus, S. Cronin, A. Gomes Souza Filho, in: Solid State Properties, 2018.
[4] B. von Blanckenhagen, D. Tonova, J. Ullmann, Application of the Tauc-Lorentz formulation to the interband absorption of optical coating materials, Appl. Opt. 41 (2002) 3137–3141.
[5] L.V. Rodríguez-de Marcos, J.I. Larruquert, Analytic optical-constant model derived from Tauc-Lorentz and Urbach tail, Opt. Express 24 (2016) 28561–28572.
[6] K. Tamura, K. Hirakawa, Y. Shimada, Drude absorption and electron localization in GaAs/AlGaAs superlattices, Phys. B Condens. Matter. 272 (1999) 183–186.
[7] D. Svintsov, V. Ryzhii, T. Otsuji, Negative dynamic Drude conductivity in pumped graphene, Appl. Phys. Express 7 (2014) 115101.
[8] C. Singh, S. Nozaki, S. Rath, Spectroscopic ellipsometry study of the free-carrier and band-edge absorption in ZnO thin films: effect of non-stoichiometry, J. Appl. Phys. 118 (2015) 195305.
[9] X. Chen, L. Liu, P.Y. Yu, S.S. Mao, Increasing solar absorption for photocatalysis with black hydrogenated titanium dioxide nanocrystals, Science 331 (2011)

746–750 (80).
[10] H. Fujiwara, M. Kondo, Effects of carrier concentration on the dielectric function of ZnO: Ga and In_2O_3: Sn studied by spectroscopic ellipsometry: analysis of free-carrier and band-edge absorption, Phys. Rev. B. 71 (2005) 75109.
[11] A.M. Stoneham, P.J. Durham, The ordering of crystallographic shear planes: theory of regular arrays, J. Phys. Chem. Solids. 34 (1973) 2127–2135.
[12] L. Liborio, G. Mallia, N. Harrison, Electronic structure of the Ti_4O_7 Magnéli phase, Phys. Rev. B. 79 (2009) 245133.
[13] M. Watanabe, Raman spectroscopy of charge-ordered states in Magnéli titanium oxides, Phys. Status Solidi. 6 (2009) 260–263.
[14] H.K. Ardakani, Electrical and optical properties of in situ "hydrogen-reduced" titanium dioxide thin films deposited by pulsed excimer laser ablation, Thin Solid Films 248 (1994) 234–239.
[15] A. O'Hara, T.N. Nunley, A.B. Posadas, S. Zollner, A.A. Demkov, Electronic and optical properties of NbO_2, J. Appl. Phys. 116 (2014) 213705.
[16] Z. Weibin, W. Weidong, W. Xueming, C. Xinlu, Y. Dawei, S. Changle, P. Liping, W. Yuying, B. Li, The investigation of NbO_2 and Nb_2O_5 electronic structure by XPS, UPS and first principles methods, Surf. Interface Anal. 45 (2013) 1206–1210.
[17] V. Eyert, The metal-insulator transition of NbO_2: An embedded Peierls instability, EPL Europhys. Lett. 58 (2002) 851.
[18] F.J. Wong, N. Hong, S. Ramanathan, Orbital splitting and optical conductivity of the insulating state of NbO_2, Phys. Rev. B. 90 (2014) 115135.
[19] J. Zhang, K.J. Norris, G. Gibson, D. Zhao, K. Samuels, M.M. Zhang, J.J. Yang, J. Park, R. Sinclair, Y. Jeon, Z. Li, R.S. Williams, Thermally induced crystallization in NbO_2 thin films, Nature 6 (2016) 34294.
[20] K. Sakata, Study of the phase transition in $Nb_xTi_{1-x}O_2$, J. Phys. Soc. Jpn. 26 (1969) 1067.
[21] K. Sakata, Structural features of $Nb_xTi_{1-x}O_2$, Acta Crystallogr. Sect. B. 35 (1979) 2836–2842.
[22] J. Arbiol, J. Cerdà, G. Dezanneau, A. Cirera, F. Peiró, A. Cornet, J.R. Morante, Effects of Nb doping on the TiO_2 anatase-to-rutile phase transition, J. Appl. Phys. 92 (2002) 853–861.
[23] T. Hitosugi, H. Kamisaka, K. Yamashita, H. Nogawa, Y. Furubayashi, S. Nakao, N. Yamada, A. Chikamatsu, H. Kumigashira, M. Oshima, Y. Hirose, T. Shimada, T. Hasegawa, Electronic band structure of transparent conductor: Nb-doped anatase TiO_2, Appl. Phys. Express. 1 (2008) 111203.
[24] Y. Furubayashi, T. Hitosugi, Y. Yamamoto, K. Inaba, G. Kinoda, Y. Hirose, T. Shimada, T. Hasegawa, A transparent metal: Nb-doped anatase TiO_2, Appl. Phys. Lett. 86 (2005) 252101.
[25] A. Ishii, K. Kobayashi, I. Oikawa, A. Kamegawa, M. Imura, T. Kanai, H. Takamura, Low-temperature preparation of rutile-type TiO_2 thin films for optical coatings by aluminum doping, Appl. Surf. Sci. 412 (2017) 223–229.
[26] H. Perron, C. Domain, J. Roques, R. Drot, E. Simoni, H. Catalette, Optimisation of accurate rutile TiO_2 (110), (100), (101) and (001) surface models from periodic DFT calculations, Theor. Chem. Acc. 117 (2007) 565–574.
[27] B.X. Huang, K. Wang, J.S. Church, Y.-S. Li, Characterization of oxides on niobium by raman and infrared spectroscopy, Electrochim. Acta 44 (1999) 2571–2577.
[28] Y. Zhao, Z. Zhang, Y. Lin, Optical and dielectric properties of a nanostructured NbO_2 thin film prepared by thermal oxidation, J. Phys. D. 37 (2004) 3392.
[29] B.J. Stagg, T.T. Charalampopoulos, Surface-roughness effects on the determination of optical properties of materials by the reflection method, Appl. Opt. 30 (1991) 4113–4118.
[30] D.E. Aspnes, A.A. Studna, Dielectric functions and optical parameters of Si, Ge, GaP, GaAs, GaSb, InP, InAs, and InSb from 1.5 to 6.0 eV, Phys. Rev. B. 27 (1983) 985–1009.
[31] J. Pflüger, J. Fink, W. Weber, K.P. Bohnen, G. Crecelius, Dielectric properties of TiC_x, TiN_x, VC_x, and VN_x from 1.5 to 40 eV determined by electron-energy-loss spectroscopy, Phys. Rev. B. 30 (1984) 1155–1163.
[32] M.R. Querry, Optical Constants, Kansas City, 1985.
[33] N. Mufti, T. Atma, A. Fuad, E. Sutadji, Synthesis and characterization of black, red and yellow nanoparticles pigments from the iron sand, AIP Conf. Proc. 1617 (2014) 165–169.
[34] X. Zhang, A. Bradley, L.N. Thibos, Achromatizing the human eye: the problem of chromatic parallax, J. Opt. Soc. Am. A. 8 (1991) 686–691.
[35] J. Tauc, Optical properties and electronic structure of amorphous Ge and Si, Mater. Res. Bull. 3 (1968) 37–46.
[36] E.A. Davis, N.F. Mott, Conduction in non-crystalline systems V. Conductivity, optical absorption and photoconductivity in amorphous semiconductors, Philos. Mag. A J. Theor. Exp Appl. Phys. 22 (1970) 903–922.
[37] I. Bonalde, E. Medina, M. Rodríguez, S.M. Wasim, G. Marín, C. Rincón, A. Rincón, C. Torres, Urbach tail, disorder, and localized modes in ternary semiconductors, Phys. Rev. B. 69 (2004) 195201.
[38] S.J. Ikhmayies, R.N. Ahmad-Bitar, A study of the optical bandgap energy and Urbach tail of spray-deposited CdS: In thin films, J. Mater. Res. Technol. 2 (2013) 221–227.
[39] B.D. Viezbicke, S. Patel, B.E. Davis, D.P. Birnie III, Evaluation of the Tauc method for optical absorption edge determination: ZnO thin films as a model system, Phys. Status Solidi. 252 (2015) 1700–1710.
[40] S. Tanemura, L. Miao, P. Jin, K. Kaneko, A. Terai, N. Nabatova-Gabain, Optical properties of polycrystalline and epitaxial anatase and rutile TiO_2 thin films by rf magnetron sputtering, Appl. Surf. Sci. 212–213 (2003) 654–660.
[41] J. Nakahara, K. Kobayashi, A. Fujii, Indirect-Forbidden Transitions in TlCl and TlBr, J. Phys. Soc. Jpn. 37 (1974) 1312–1318.
[42] A. Schlegel, S.F. Alvarado, P. Wachter, Optical properties of magnetite (Fe_3O_4), J. Phys. C Solid State Phys. 12 (1979) 1157.
[43] Ellingham Diagram, Encycl. Inorg. Bioinorg. Chem. (2011), https://doi.org/10.1002/9781119951438.eibd0278.
[44] S.A. Chambers, Y. Gao, Y.J. Kim, M.A. Henderson, S. Thevuthasan, S. Wen, K.L. Merkle, Geometric and electronic structure of epitaxial $Nb_xTi_{1-x}O_2$ on TiO_2(110), Surf. Sci. 365 (1996) 625–637.